



HAL
open science

Computational analysis of flow structures in turbulent ventricular blood flow associated with mitral valve intervention

Joel Kronborg, Frida Svelander, Samuel Eriksson-Lidbrink, Ludvig Lindström, Carme Homs-Pons, Didier Lucor, Johan Hoffman

► **To cite this version:**

Joel Kronborg, Frida Svelander, Samuel Eriksson-Lidbrink, Ludvig Lindström, Carme Homs-Pons, et al.. Computational analysis of flow structures in turbulent ventricular blood flow associated with mitral valve intervention. 2021. hal-03443780

HAL Id: hal-03443780

<https://hal.science/hal-03443780>

Preprint submitted on 23 Nov 2021

HAL is a multi-disciplinary open access archive for the deposit and dissemination of scientific research documents, whether they are published or not. The documents may come from teaching and research institutions in France or abroad, or from public or private research centers.

L'archive ouverte pluridisciplinaire **HAL**, est destinée au dépôt et à la diffusion de documents scientifiques de niveau recherche, publiés ou non, émanant des établissements d'enseignement et de recherche français ou étrangers, des laboratoires publics ou privés.

Computational analysis of flow structures in turbulent ventricular blood flow associated with mitral valve intervention

Joel Kronborg^{1,*}, Frida Svelander¹, Samuel Eriksson-Lidbrink¹, Ludvig Lindström¹, Carme Homs-Pons¹, Didier Lucor² and Johan Hoffman¹

¹*KTH Royal Institute of Technology, Department of Computational Science and Technology, School of Electrical Engineering and Computer Science, Stockholm, Sweden*

²*Laboratoire Interdisciplinaire des Sciences du Numérique, LISN-CNRS, Orsay, France*

Correspondence*:
Joel Kronborg
joelkro@kth.se

2 ABSTRACT

3 Cardiac disease and clinical intervention may both lead to an increased risk for thrombosis
4 events due to a modified blood flow in the heart, and thereby a change in the mechanical
5 stimuli of blood cells passing through the chambers of the heart. Specifically, the degree of
6 platelet activation is influenced by the level and type of mechanical stresses in the blood flow. In
7 this article we analyze the blood flow in the left ventricle of the heart through a computational
8 model constructed from patient-specific data. The blood flow in the ventricle is modeled by the
9 Navier-Stokes equations, and the flow through the mitral valve by a parameterized model which
10 represents the projected opening of the valve. A finite element method is used to solve the
11 equations, from which a simulation of the velocity and pressure of the blood flow is constructed.
12 The intraventricular blood flow is complex, in particular in diastole when the inflow jet from the
13 atrium breaks down into turbulent flow on a range of scales. A triple decomposition of the velocity
14 gradient tensor is then used to distinguish between rigid body rotational flow, irrotational straining
15 flow, and shear flow. The triple decomposition enables the separation of three fundamentally
16 different flow structures, that each generates a distinct type of mechanical stimulus on the blood
17 cells in the flow. We compare the results to a simulation where a mitral valve clip intervention is
18 modelled, which leads to a significant modification of the ventricular flow. Further, we perform
19 a sensitivity study of the results with respect to the positioning of the clip. It was found that the
20 shear in the simulation cases treated with clips increased more compared to the untreated case
21 than the rotation and strain did. A decrease in valve opening area of 64 % in one of the cases
22 led to a 90 % increase in rotation and strain, but a 150 % increase in shear. The computational
23 analysis suggests a process for patient-specific simulation of clinical interventions in the heart
24 with a detailed analysis of the resulting blood flow, which could support clinical risk assessment
25 with respect to platelet activation and thrombosis events.

26 **Keywords:** patient-specific heart modelling, left ventricle, mitral valve clip, finite element method, turbulent blood flow, triple
27 decomposition of velocity gradient tensor

1 INTRODUCTION

28 Heart attack and stroke follow from a loss of blood supply to the heart and brain, respectively, often caused
29 by a blood clot that obstructs a critical blood vessel, referred to as thrombosis. Blood clots are naturally
30 formed as a response to injury to avoid blood loss, but may also form under other circumstances where the
31 platelets (thrombocytes) of the blood are activated which leads to an increased tendency of the platelets to
32 aggregate, see e.g., Previtali et al. (2011). Platelet activation can be triggered by contact with a foreign
33 material, such as a medical device, see e.g., Rojano et al. (2019), or by the mechanical stresses in the
34 blood flow. Specifically, it is associated with elevated levels of shear in the blood. The degree and time
35 extent of the activation is a function of the type of mechanical stimulus experienced by the platelets, see
36 e.g., Rahman et al. (2020). Therefore, a detailed analysis of the structure of the blood flow may help to
37 assess the risk for platelet activation and thrombosis. The heart is supplied blood through the right and
38 left coronary arteries, with inlets through the right and left coronary sinuses which are part of the aortic
39 root attached to the left ventricle (LV) of the heart. Further downstream the aorta, the brain is supplied
40 blood through the carotid arteries that emanate from the aortic arch. As a consequence, the level of platelet
41 activation in the LV blood flow is of interest when assessing the risk for thrombosis events in both the heart
42 and the brain.

43 Blood flow in the LV is complex, in particular in diastole when the heart relaxes and blood flows into
44 the ventricle from the left atrium through the open mitral valve. The ventricular blood flow is also highly
45 sensitive to the structure and function of the mitral valve, and pathologies such as mitral valve regurgitation
46 or stenosis can drastically change the flow pattern. In the early filling phase of diastole (the E-wave) a jet
47 is formed which then breaks down in the diastasis phase, after which a second jet is formed in the atrial
48 contraction phase (the A-wave). The two successive jets create shear layers and vortex rings in the ventricle,
49 which then break down into turbulent flow structures on a range of scales. The blood flow generates
50 mechanical stimuli on blood cells that trigger different responses in the cells, for example, activation
51 of platelets. Mechanical stimuli on blood cells are difficult or impossible to assess by medical imaging
52 alone, and the turbulent nature of the ventricular flow makes this challenge even greater. In this article we
53 investigate to what degree a computational model can be used to assess the mechanical stimuli on blood
54 cells in the LV flow, building on our previous work on patient specific simulations of the LV blood flow,
55 see e.g., Larsson et al. (2017b) and Larsson et al. (2017a), and analysis of turbulent flow structures, see
56 Hoffman (2021).

57 Cardiac disease and clinical interventions may both lead to changes in the LV blood flow and the
58 mechanical stimuli experienced by the blood cells in the ventricle. Mitral valve regurgitation is a condition
59 which affects the LV blood flow, where the mitral valve does not close properly and therefore may leak in
60 systole when the valve is supposed to be closed. A common procedure to mitigate mitral valve regurgitation
61 is to suture the two leaflets of the mitral valve together with a mitral valve clip (MVC). While a MVC
62 intervention reduces or removes the regurgitation, there is a risk for creating a new problem in the form
63 of stenosis, due to a reduced valve opening. Recently, patient-specific computer simulations have been
64 used to evaluate the risks and benefits of a MVC intervention, see Caballero et al. (2020). In this article we
65 use a finite element method to simulate the blood flow in the LV before and after a MVC intervention, to
66 analyze the difference in the ventricular blood flow. We also perform a sensitivity study with respect to
67 the positioning of the MVC. A two dimensional model of the mitral valve is used, which represents an
68 approximation of the projected opening between the left atrium and the left ventricle. The mitral valve
69 model is then modified to take the positioning of the MVC into account.

70 To analyze the simulated blood flow we use the triple decomposition of the velocity gradient tensor,
 71 suggested by Kolář (2007) to improve the identification and visualization of vortices. Hoffman (2021)
 72 noted that the triple decomposition implies that the flow locally can be approximated by a sum of shear
 73 flow, rigid body rotational flow and irrotational straining flow. Our hypothesis is that this refined analysis
 74 of the blood flow will lead to an improved quantification of the type and extent of the mechanical stresses
 75 experienced by blood cells while inside the LV, which can support a risk assessment of thrombosis events
 76 to a greater extent than a blood flow analysis based solely on the velocity and pressure of the blood.

77 In Section 2 we describe the computational model and the triple decomposition of the velocity gradient
 78 tensor, and in Section 3 we present results from the simulations. These results are then discussed in
 79 Section 4.

2 METHOD

80 2.1 Left ventricle model

81 The LV model is based on 4D transthoracic echocardiography (TTE) images of the left ventricle of one
 82 human subject, acquired using the technique described in detail in Larsson et al. (2017b). Images were
 83 captured in 26 frames over a full cardiac cycle which lasted for 830 ms, and the heart wall was segmented
 84 in a semi-automated fashion in each image, see Hansegård et al. (2009). From this a set of triangulated
 85 surface meshes were generated which described the deformation of the endocardium over the cardiac cycle.

86 The orifice of the mitral valve (MV) was identified by a sonographer in thirteen 2D short axis B-mode
 87 views in early diastole, with each view rotated 15 degrees around the LV long axis. Similarly, the aortic
 88 valve opening was identified in a single 3-chamber B-mode view in early systole. Both valve openings
 89 were marked on the surface meshes.

90 From one surface mesh corresponding to end diastole, here referred to as the initial surface mesh, a refined
 91 version was produced, from which a tetrahedral volume mesh of the interior of the ventricle was generated.
 92 This volume mesh consists of 406,964 vertices. This resolution was chosen based on the convergence
 93 studies in Larsson et al. (2017b), which showed less than 2 % deviation in results when increasing mesh
 94 resolution above 400,000 vertices.

95 2.2 Simulation of blood flow

96 The blood in the LV is modelled as an incompressible Newtonian fluid. Although blood is known to
 97 express non-Newtonian properties in smaller blood vessels, see e.g., Pedley and Fung (1980), and Adjoua
 98 and Lucor (2019), the blood inside the heart chambers is typically modelled as a Newtonian fluid, see
 99 Westerhof et al. (2010). To simulate the LV blood flow, we determine the velocity vector $\mathbf{u}(\mathbf{x}, t) : \Omega^t \rightarrow \mathbb{R}^3$
 100 and scalar pressure $p(\mathbf{x}, t) : \Omega^t \rightarrow \mathbb{R}$, such that the Navier-Stokes equations are satisfied:

$$\rho(\dot{\mathbf{u}} + (\mathbf{u} \cdot \nabla)\mathbf{u}) - \mu\Delta\mathbf{u} + \nabla p = 0, \quad (\mathbf{x}, t) \in \Omega^t \times [0, T] \quad (1)$$

$$\nabla \cdot \mathbf{u} = 0, \quad (\mathbf{x}, t) \in \Omega^t \times [0, T], \quad (2)$$

101 defined over the time-dependent domain $\Omega^t \subset \mathbb{R}^3$ at time $t \in [0, T]$. Equation (1) expresses conservation
 102 of momentum, and equation (2) conservation of mass. Standard mathematical notation is used, with ∇ the
 103 gradient operator and Δ the Laplacian operator. We use the dynamic viscosity $\mu = 0.0027$ Pa·s and the
 104 blood density $\rho = 1060$ kg/m³, see Di Martino et al. (2001).

105 Ω^t represents the deforming LV, with the boundary $\partial\Omega^t$ partitioned into the heart wall and the two valve
 106 orifices. We use no slip velocity boundary conditions, corresponding to setting the blood flow velocity
 107 equal to the deformation velocity of the heart wall and closed valves. In systole, the open aortic valve (AV)
 108 is modelled by a standard outflow boundary condition, where the pressure is set to zero. The model of the
 109 mitral valve is described below, with and without a MVC intervention. To simulate the LV blood flow over
 110 the cardiac cycle, the domain Ω^t is approximated by the tetrahedral volume mesh which is deformed over
 111 time based on the 26 surface meshes. For a detailed description of this process, see Larsson et al. (2017b).
 112 The Navier-Stokes equations are solved on this deforming volume mesh using an arbitrary Lagrangian-
 113 Eulerian (ALE) formulation of a stabilized finite element method, which is described in Hiromi Spühler
 114 and Hoffman (2021).

115 2.3 Mitral valve model

116 We extend the LV model with a simple planar, data-driven parameterized model of the MV dynamics,
 117 which acts as a time dependent inflow boundary condition. The MV is modeled as a time-varying orifice
 118 representing the area enclosed by the planar projection of the leaflets onto the mitral annulus, accounting
 119 for virtual folding/unfolding mitral leaflets, similar to the work in Imanparast et al. (2016).

120 The basic shape of the annulus is modeled as two half ellipses sharing a common long axis. From the
 121 ultrasound identification of the MV, the length of the long axis and the two short axes are identified, as well
 122 as the spatial 2D location of the coaptation line within the annulus area. An MV center point on the wall of
 123 the ventricle mesh is also given from the TTE images, which is used as a spatial reference point on the
 124 mesh to keep the MV in place. In figure 1a the MV and AV areas on the simulation mesh are displayed, as
 125 well as the contour of the MV model and the projected leaflets for a particular moment in time in figure 1b.

126 The opening and closing of the MV are given as temporal variations of the short axes of the two half
 127 ellipses. During systole, the short axes are equal, effectively keeping the projection of the leaflet edges
 128 overlapped along the coaptation line. Throughout diastole, the short axes are scaled to imitate a projection
 129 of the moving leaflets onto the surface mesh. Effectively this corresponds to a maximum opening area at
 130 E-wave peak, slightly smaller in diastasis, and somewhere in between at A-wave peak. For these points
 131 in time in the diastole timeline, the short axis scalings are determined by an idealized MV, see Fyrenius
 132 et al. (2001). Patient-specific scalings are difficult to determine from echocardiography images since the
 133 resolution is limited. The predetermined scale factors are given in table 1 for E-wave peak, diastasis start
 134 and end, and A-wave peak.

Table 1. Timings of different parts of diastole, and scalings of the short axis anterior (SAA) and short axis posterior (SAP) of the MV model at those times. The timings are determined by analyzing changes in the rate of expansion of the LV. Note that the coaptation line does not coincide with the intercommissural line (long axis), but the scalings at diastole start and end correspond to both leaflet edges coinciding with the coaptation line, i.e. the MV is closed at these times.

	Diastole start	E-wave peak	Diastasis start	Diastasis end	A-wave peak	Diastole end
t (s)	0.420	0.525	0.644	0.711	0.779	0.830
SAA scale	0.40	1.00	0.50	0.50	0.85	0.40
SAP scale	-0.57	1.00	0.70	0.70	0.85	-0.57

135 Although the patient-specific scaling of the short axes could not be determined from the echocardiography
 136 images, the timings for the E-wave and A-wave peaks, as well as diastasis start and end, are determined

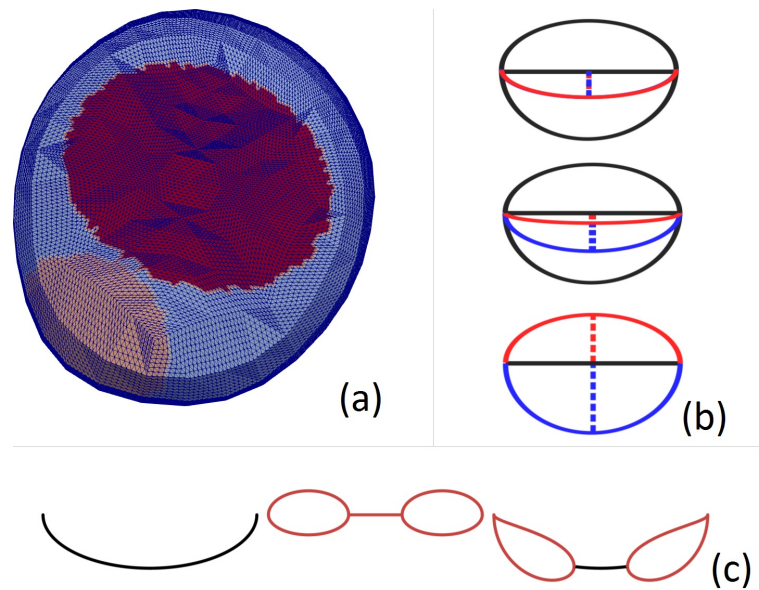


Figure 1. (a) AV placement (yellow) and MV placement (red) on the LV surface mesh in an axial view. (b) The two half ellipses making up the MV model at different stages throughout the heartbeat cycle. The solid red line is the projection of the anterior leaflet, and the solid blue line the posterior. The dashed lines are the short axes of the corresponding half ellipse. In the top view the valve is fully closed (systole), and the leaflets overlap on the coaptation line. In the bottom view the valve is fully open (E-wave peak), and the center view shows early diastole. The solid black line through the valve model is the long axes of the two half ellipses. (c) The coaptation line (left), the two double half ellipses making up the MV model after MVC intervention (center) and the final shape of the MV model after MVC intervention (right). The part that does not open is the location of the clip.

137 based on the expansion rate of the LV of the particular subject studied here. This can be done patient
 138 specifically for other cases as well.

139 The volumes of the 26 frames extracted from the echocardiography images are displayed in figure 2,
 140 plotted against time from the beginning of systole. A cubic smoothing spline curve, $V(t)$ is fitted to the
 141 data points. From the first and second derivative (also included in figure 2) of this smooth curve the timings
 142 are identified. Fundamentally, the shift from systole to diastole is identified as the point where the first
 143 derivative dV/dt (i.e. the rate of the volume change) is 0, shifting from negative (contraction) to positive
 144 (expansion). The shift from diastole to systole is given simply as the beginning/end time of this heartbeat.
 145 Note that the isovolumetric phases between diastole and systole are excluded for simplicity.

146 The E-wave and A-wave peaks are easily identified as the local maxima in dV/dt , with E-wave peak
 147 being the former and higher one. To define diastasis, the local minimum between these two peaks is
 148 determined. Diastasis is then defined as the time between the two original data frames from the TTE images
 149 on either side of this local minimum. These timings are listed in table 1.

150 With the timings of these four crucial points determined, along with the timings for shifts from diastole
 151 to systole and vice versa, the scaling of the short axes of the MV model are given by cubic Hermite
 152 interpolation between the scaled axis lengths and times given in table 1. The resulting axes scaling over the
 153 full duration of diastole is displayed in figure 3.

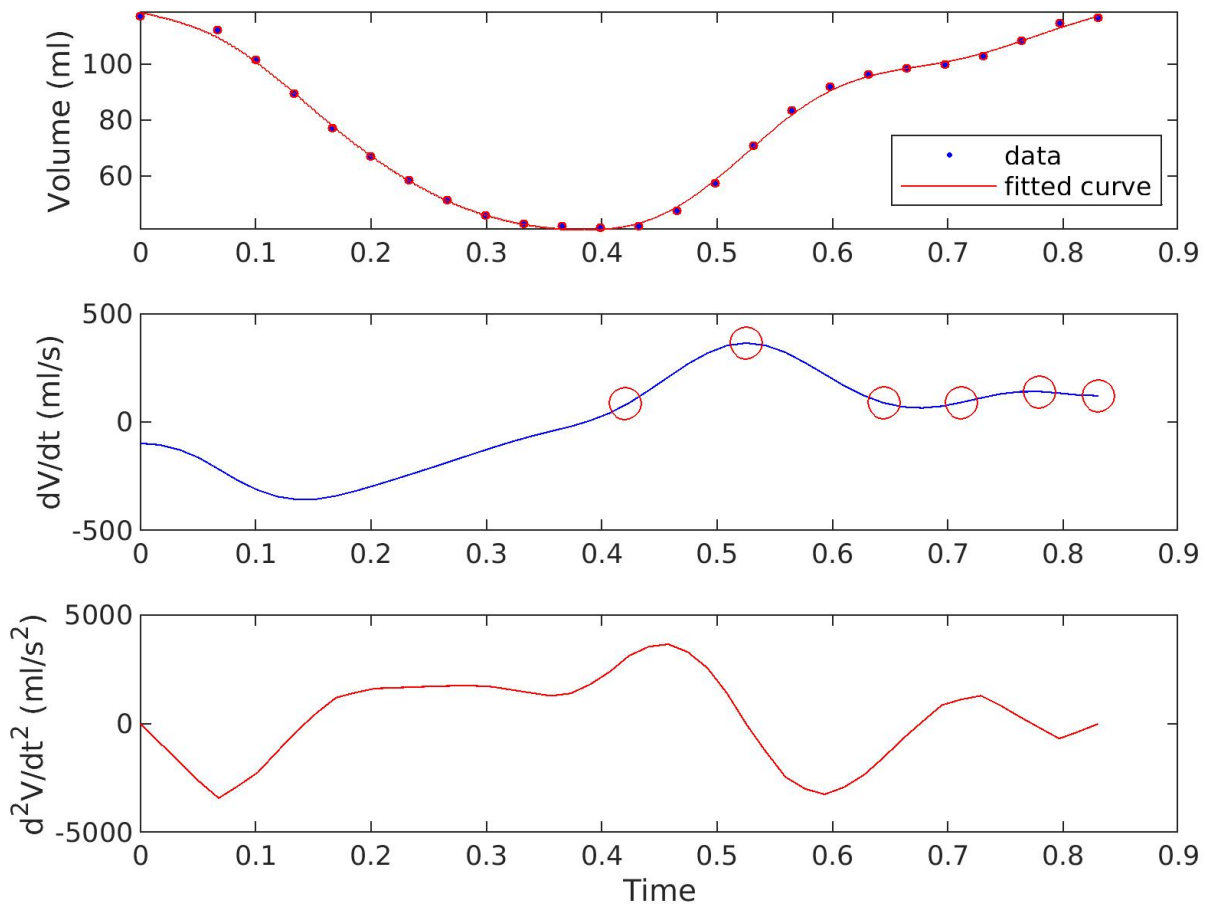


Figure 2. Volume of the acquired surface meshes of the LV, and the first and second derivative of the interpolated curve. The top plot shows the volumes of the 25 used frames directly from the TEE images as blue dots, and the interpolation as a red line. The middle plot shows the first derivative, and the resulting timings of diastole start, E-wave peak, diastasis start and end, A-wave peak, and diastole end as red circles (see table 1 for exact values). The bottom plot shows the second derivative.

154 2.3.1 After mitral valve clip intervention

155 To simulate the inflow of blood after a MVC intervention, part of the coaptation line of the MV was
 156 kept stationary in its closed state throughout diastole. This produces a valve model with two smaller
 157 openings, one on either side of the clip as displayed in figure 1c. This is achieved by creating two smaller
 158 openings consisting of two half ellipses each, similar to the untreated case, and superpositioning this with
 159 the coaptation line. The two smaller openings behave much like smaller versions of the untreated MV
 160 model throughout diastole. They follow the same pattern for opening and closing, i.e. the same scalings
 161 and timings given in table 1. In its closed state, the clipped MV model has the same coaptation line as the
 162 untreated valve model.

163 Since the length of the coaptation line is the same for the clipped and untreated models, the long axes
 164 of the two smaller openings are directly given from the remaining unclipped parts. Additionally, the
 165 relationship between the anterior and posterior short axis of each opening is the same as the relationship of

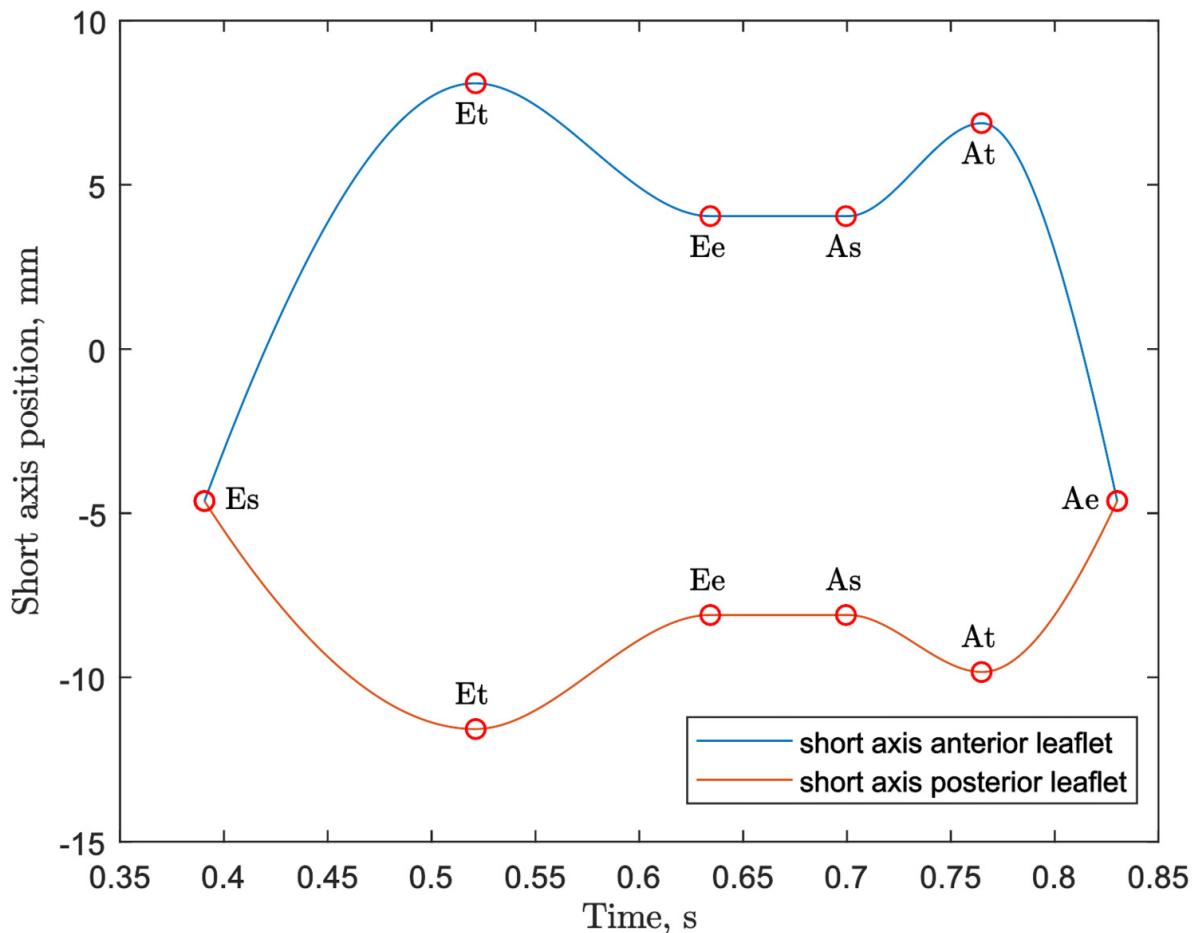


Figure 3. Lengths of the short axes of the anterior (blue) and posterior (red) leaflets in the MV model over time. The times marked by red circles are E-wave start (Es), E-wave peak (Et), E-wave end/diastasis start (Ee), A-wave start/diastasis end (As), A-wave peak (At) and A-wave end (Ae). The times and scalings of the short axes are given in table 1.

166 the short axes in the untreated case. The length of the two anterior short axes are assumed to have the same
 167 relationship as the length of their corresponding long axes, and the same holds for the posterior short axes.

168 To compute the maximum length of the short axes in the MVC case, the length of the edge of the
 169 openings at E-wave peak is assumed to be the same as the length of the edges in the untreated case, i.e. the
 170 circumference of the orifice. Along with the relationships between different axes described above, this is
 171 used to uniquely determine the maximum length of the short axes. As in the untreated case, this is assumed
 172 to imitate a projection of the 3D MV opening onto the surface mesh of the ventricle, see Imanparast et al.
 173 (2016). Given the length of the ellipse axes and the MVC, the total area of the two openings were computed
 174 and are presented in table 2.

175 2.4 Simulations

176 Five different cases were simulated, with MVC centers positioned along the coaptation line at $s \cdot l$ from
 177 the coaptation line center, with l being the same long axis length as used in the untreated valve, i.e. half the
 178 intercommissural distance, and $s \in (-1, 1)$ a scaling parameter. The values of s used in these simulations

179 are given in table 2, along with the resulting MV opening areas at mid diastole. Hence, $s = 0$ corresponds
 180 to the clip being in the center of the valve and $s = \pm 1$ to it being on the posteromedial/anterolateral
 181 commissure of the valve respectively.

Table 2. Position scale constants for the MVC simulations and resulting MV opening areas at E-wave peak. The MVC is positioned at $s \cdot l$ from the center of the coaptation line, with l being the length of the long axis in the MV model. Here $s < 0$ corresponds to clip positions anterolaterally of the center, and $s > 0$ posteromedially. For reference, the area of the MV opening at mid diastole with no MVC is 2.54 cm².

s	-0.4	-0.2	0.0	0.2	0.4
Area (cm ²)	1.08	0.93	0.86	0.93	1.08

182 In addition to the five cases with the MVC in different positions, one case with an untreated valve was
 183 also simulated using the original MV model. Note that the untreated valve was modeled without any
 184 regurgitation. This is a model simplification motivated by the fact that our focus is to compare the blood
 185 flow into the ventricle during diastole. In this model the inflow is not greatly affected by any regurgitation
 186 in systole. The significant difference is that between the flow in the different double orifice cases in MVC
 187 treated valves and the single orifice of the untreated valve.

188 The LV used in these simulations has a volume at end diastole of 117 ml, and an ejection fraction of 64 %.
 189 These values, as well as the deformation of the ventricle volume throughout the heartbeats, are the same in
 190 all simulations. The untreated MV has a long axis of 12.8 mm, and short axes of 11.6 mm (posterior) and
 191 8.1 mm (anterior) respectively. This results in an opening area of 4.0 cm² at E-wave peak, and 2.54 cm² at
 192 mid diastole. This is a relatively small opening area, so the resulting velocities and pressures in the MVC
 193 simulations are likely higher than a typical *in-vivo* case.

194 All simulations were run on the KTH supercomputer of Technology (2021), a Cray XC40 system with
 195 67,456 cores distributed over 4,120 Intel Xeon E5-269X 2.1/2.3 GHz CPUs. The simulations were run for
 196 six heartbeats, starting from early systole, all with identical wall motion from the captured TTE images.
 197 The time step length was set to 1 ms. One of the 26 surface meshes generated from the TTE data diverged
 198 significantly from the others, and was thus considered an outlier and excluded from the simulations.
 199 Between the rest of the captured frames, the surface meshes were temporally interpolated using cubic
 200 Hermite interpolation, to yield one surface mesh for each simulated time step.

201 2.5 Blood flow analysis

202 To analyze the blood flow in the ventricle we can visualize the flow velocity and pressure computed from
 203 the Navier-Stokes equations. It is also useful to analyze the velocity gradient $\nabla \mathbf{u}$, a tensor which describes
 204 the local spatial change in velocity at each time and position, defined by its components

$$(\nabla \mathbf{u})_{ij} = \frac{\partial u_i}{\partial x_j}. \quad (3)$$

205 Near each point $\mathbf{x}_0 \in \Omega^t$, the velocity gradient can be used to construct a linear approximation

$$\mathbf{u}(\mathbf{x}) \approx \mathbf{u}(\mathbf{x}_0) + \nabla \mathbf{u}(\mathbf{x}_0)(\mathbf{x} - \mathbf{x}_0), \quad (4)$$

206 and the mechanical stresses in the blood can be derived from the velocity gradient.

207 A standard double decomposition of the velocity gradient constitutes a separation of the flow into a
 208 straining flow and a rotational flow, corresponding to its symmetric part $S(\mathbf{u})$, the strain rate tensor, and
 209 the skew-symmetric part $\Omega(\mathbf{u})$, the spin tensor:

$$\nabla \mathbf{u} = \frac{1}{2}(\nabla \mathbf{u} + (\nabla \mathbf{u})^T) + \frac{1}{2}(\nabla \mathbf{u} - (\nabla \mathbf{u})^T) = S(\mathbf{u}) + \Omega(\mathbf{u}), \quad (5)$$

210 where the superscript T represents the transpose of the tensor. The weakness of the double decomposition
 211 is that shear flow is unaccounted for. To address this shortcoming, the triple decomposition was proposed
 212 by Kolář (2007), where the velocity gradient tensor is decomposed into a sum of three parts corresponding
 213 to irrotational straining flow (compression and elongation) $(\nabla \mathbf{u})_{EL}$, rigid body rotational flow $(\nabla \mathbf{u})_{RR}$,
 214 and shear flow $(\nabla \mathbf{u})_{SH}$:

$$\nabla \mathbf{u} = Q((\nabla \mathbf{u})_{EL} + (\nabla \mathbf{u})_{RR} + (\nabla \mathbf{u})_{SH})Q^T, \quad (6)$$

215 where Q is an orthogonal matrix that represents a new frame of reference in which the shear flow can be
 216 subtracted from the other two parts. For the sake of brevity, we will refer to the three flow structures as
 217 strain, rotation and shear.

218 Algebraically, the matrix decomposition may be interpreted as a sum of a normal symmetric part, a
 219 normal skew-symmetric part, and a non-normal part, which can be computed through the real Schur
 220 decomposition of the velocity gradient tensor, see e.g., Van Loan and Golub (1996). In this article, the triple
 221 decomposition was computed by using the Matlab function *schur*, which returns a frame of reference Q
 222 that corresponds to a standardized form of the real Schur decomposition from which the shear flow tensor
 223 can be extracted, see Hoffman (2021). To determine the magnitude of each flow component, Frobenius
 224 norms of each respective matrix were computed.

3 RESULTS

225 3.1 Flow structures

226 Snapshots of the velocity magnitudes in a bicommissural vertical cut through the ventricle for all simulated
 227 cases are shown in figure 4. The snapshots are taken at time $t = 0.45$ s from the start of the analyzed
 228 heartbeat (cf. figure 3), i.e. 30 ms after the start of diastole. At this point in time inflow jets through the
 229 mitral valve can be observed in all cases. The untreated valve has a single wide jet, whereas the cases with
 230 MVC's in different positions show the double jets characteristic of inflow after MVC treatment.

231 The average velocity in the jet of the untreated case (figure 4a), which has a larger MV opening area than
 232 the others, is smaller than the velocities in the clipped cases. This single wide jet also does not reach as far
 233 down into the ventricle as the jets in the other cases. Comparing the treated cases, the one with the clip in
 234 the center of the coaptation line (figure 4d) has a slightly higher peak velocity than the others. This case
 235 is the one with the smallest total opening area, as given in table 2. In the ventricles with asymmetrically
 236 placed clips, the wider of the two jets typically reaches further into the ventricle than the smaller jet.

237 Snapshots of the pressure at the same instant and the same cut as the velocity described above are shown
 238 in figure 5. A recurring pattern of high pressure in the apical and mid-cavity parts of the ventricle is
 239 apparent in all simulated cases, with slight variations. In the untreated case (figure 5a), where the jet does
 240 not extend as far into the ventricle, the overall pressure variations are lower than in the cases with MVC's.
 241 In the MVC cases, the double jets extend to different depths in the ventricle, which can also be seen in the

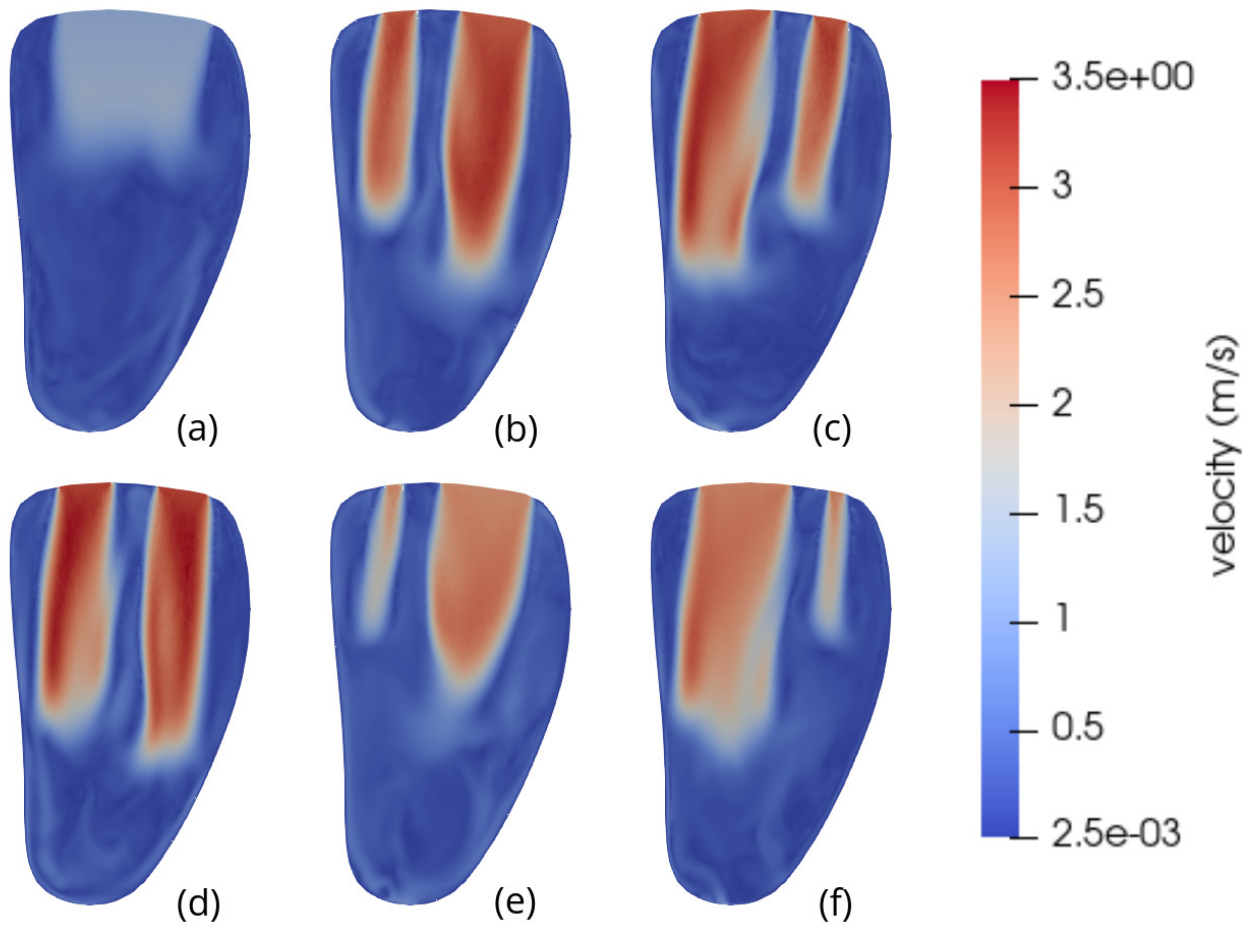


Figure 4. Snapshots of the velocity magnitude at time $t = 0.45$ s in a vertical bicommissural cut through the left ventricle. This is in early diastole before the E-wave peak, when the intraventricular blood flow is dominated by strong inflow jets. Subfigure (a) shows the untreated case. The other subfigures have MVC's positioned at $s \cdot l$ from the center, with l being the long axis of the MV model. The scale factor s for the different cases are (b) $s = -0.2$, (c) $s = 0.2$, (d) $s = 0.0$, (e) $s = -0.4$, (f) $s = 0.4$. The corresponding MV areas for each case in mid diastole are given in table 2.

242 velocity in figure 4. This makes the line between high and low pressure less straight in the MVC cases,
 243 especially when the MVC is asymmetrically positioned. High pressures just below the jets are apparent,
 244 but the lowest pressures are found around the front of the jets. This indicates the presence of vortex rings in
 245 these parts, since pressure is typically low in vortex centers.

246 3.2 Triple decomposition of velocity gradient tensor

247 Placing a clip in the MV significantly reduces the opening area of the MV, as can be seen in table 3. A
 248 natural result of this is higher inflow velocities, which the table also displays, with higher velocities the
 249 smaller the opening is. Both the velocity and the pressure are mainly affected by the reduction in area, but
 250 not so much by which side the clip is placed on. This is however not necessarily the case for the triple
 251 decomposition components, as is evident from the same table.

252 With the clip placed in the center of the MV, the opening area is the smallest out of all these simulation
 253 cases. For shear and strain, this leads to the highest computed peak values, but the peak rotation magnitude
 254 is actually slightly larger with the clip placed slightly posteromedially of the center. It is true for all three

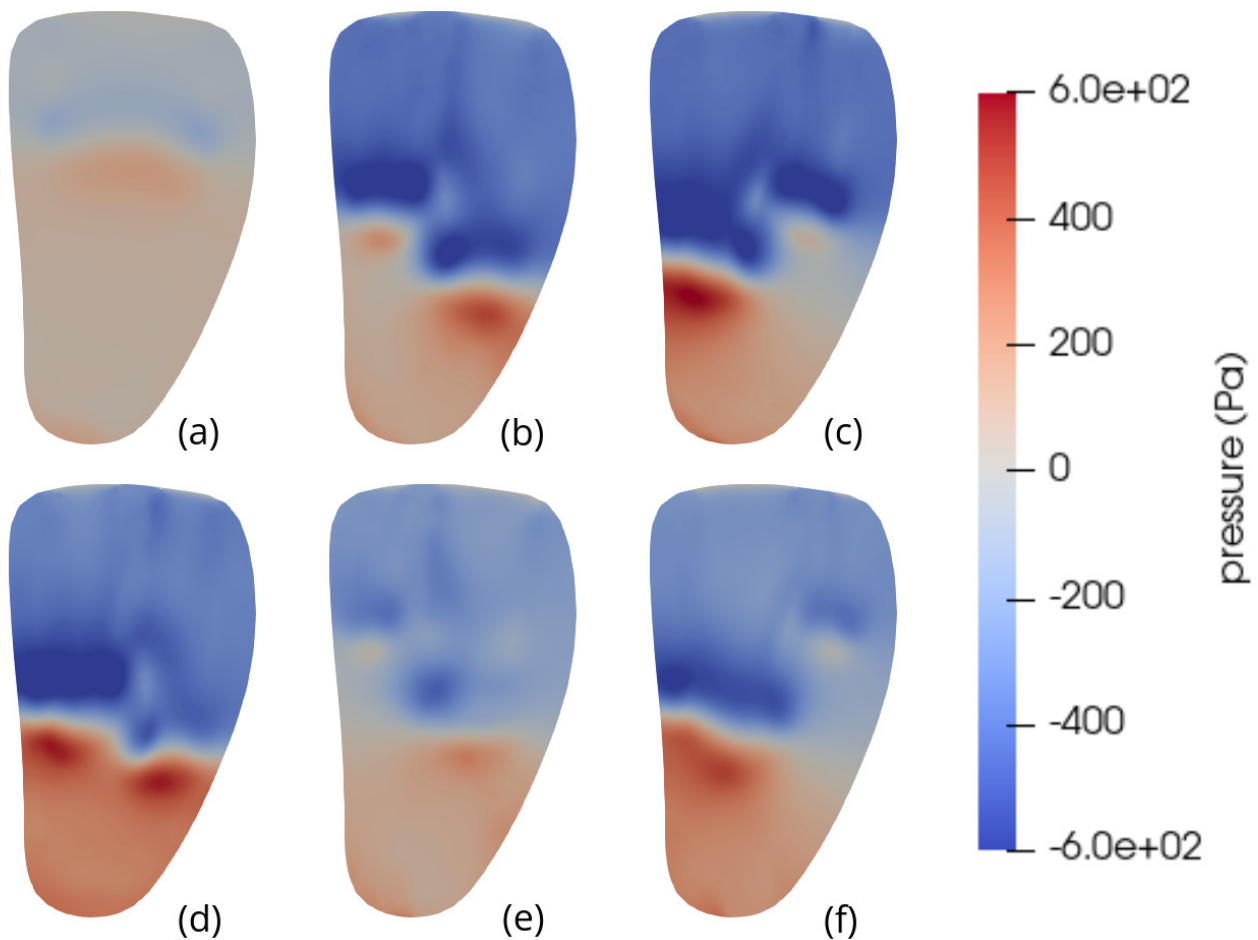


Figure 5. Snapshots of the pressure at time $t = 0.45$ s in a vertical bicommissural cut through the left ventricle. This is in early diastole before the E-wave peak, when the intraventricular blood flow is dominated by strong inflow jets. The regions just below the jets experience high pressure, while there is a pressure drop around the base of the jet. (a) shows the untreated case. The other subfigures have MVC's positioned at $s \cdot l$ from the center, with l being the long axis of the MV model. The scale factor s for the different cases are (b) $s = -0.2$, (c) $s = 0.2$, (d) $s = 0.0$, (e) $s = -0.4$, (f) $s = 0.4$. The corresponding MV areas for each case in mid diastole are given in table 2.

255 components that the peak values with the clip displaced to either side are not only dependent on how far the
 256 clip is displaced, but the direction as well. However, in most cases it does seem like smaller opening area
 257 does contribute to higher magnitudes of rotation, shear and strain, although the effect varies. The MV with
 258 the clip in the center has an opening area of 34 % of that of the untreated MV. Its peak average rotation and
 259 strain are both roughly 190 % of those for the untreated case, but its peak average shear is about 250 % of
 260 that for the untreated case. As a reference, the maximum velocity increased about twofold in the same case.
 261 Throughout all simulation cases, shear has the highest relative increase when treated with MVC, whereas
 262 rotation and strain increase roughly equally.

263 There are significant differences in how the flow in the ventricle behaves when dominated by strong
 264 inflow jets, i.e. during E-wave, and when there is no single dominating structure dictating most of the flow.
 265 Figure 6 shows snapshots of the three modalities of the triple decomposition, i.e. rotation, shear and strain,
 266 in the simulation case without the MVC. The components are displayed at two different times in diastole:
 267 $t = 0.45$ s, which corresponds to the velocities shown in figure 4, and $t = 0.71$ s, which is the time of the

Table 3. Peak values in the untreated simulation case, and the corresponding values for each of the MVC cases. Area is given at mid diastole. Velocity and pressure are the maximum values reached anywhere in the LV at E-wave peak. Rotation, shear and strain are the maxima reached in figure 8.

Simulation case	untreated	-0.4	-0.2	0.0	0.2	0.4
Area at mid diastole (cm ²)	2.54	1.08	0.93	0.86	0.93	1.08
E-wave peak velocity (m/s)	1.86	2.84	3.53	3.76	3.51	2.84
E-wave peak pressure (kPa)	0.667	2.396	3.631	4.640	3.621	2.993
Peak average rotation (s ⁻¹)	21	35.4	37.0	39.8	39.9	34.1
Peak average shear (s ⁻¹)	174.6	344.8	397.5	439.1	409.7	368.7
Peak average strain (s ⁻¹)	51.4	82.5	86.7	95.3	93.6	81.3

268 end of diastasis. Thus the first snapshots (figure 6a, c and e) show the triple decomposition at a point in
 269 time when the flow is dominated by the strong inflow through the MV in early diastole, and the second
 270 snapshots capture the components after the initial E-wave jet has broken down into smaller flow structures
 271 in the ventricle.

272 At $t = 45$, it is clear that different flow modalities are prevalent in different parts of the ventricle. Rotation
 273 (figure 6c) appears in small connected areas in the lower part of the ventricle, but notably also on either
 274 side of the lower part of the jet structure, showing the presence of a vortex ring forming around the jet.
 275 Within the jet itself, where the flow is roughly unidirectional, the rotation is 0.

276 Shear (figure 6a) at the same moment is high at the outer edge of the jet, and along the lower wall of
 277 the ventricle. There are weaker shear structures throughout much of the rest of the ventricle as well, but
 278 none within the jet. Strain (figure 6e) is also large along the wall around the apical part of the ventricle.
 279 Additionally, below the jet, at the front of the blood flowing into the ventricle from the atrium, straining
 280 flow is high. There are also smaller spots throughout the ventricle with relatively high or low strain.

281 At $t = 71$, when the E-wave jet has diminished and there is no single strong feature dominating the flow
 282 field, the overall distribution of the different flow modalities is more mixed. Rotation (figure 6d) is loosely
 283 connected in structures throughout the ventricle. Shear (figure 6b) and strain (figure 6f) are still relatively
 284 large along the ventricle wall around the apex, but the shear now also extends to other parts of the wall. In
 285 some structures near the wall but extending into the interior of the ventricle the strain is relatively high.

286 When it comes to the cases treated with MVC's, some of the appearing flow structures share similarities
 287 with those in the untreated case. Snapshots of rotation, shear and strain for the MVC case with position
 288 scaling $s = 0.2$ (corresponding to case c in figures 4 and 5) are displayed in figure 7. The snapshots are
 289 taken at the same moments in time as the ones in figure 6, and show the same cut through the ventricle.
 290 Note however the different scales for shear and strain.

291 With the flow profile dominated by two jets, as in early diastole in figure 7a, c and e, the rotation (c)
 292 again shows structures reminiscent of vortex rings around the lower part of the jets. (For the corresponding
 293 velocity snapshot, see figure 4c.) However, the magnitude of the vortex rings appear larger for the parts in
 294 the interior of the ventricle than where the jet runs close to the wall.

295 Along the edges of the jets, high shear is visible in the clipped case as well (figure 7a). The shear of
 296 the wider jet seems to extend into the center of the jet as well, but this is because the displayed cut is not
 297 perfectly through the center of the jet. Like in the untreated case, there is also significant shear along the
 298 wall in the lower part of the ventricle.

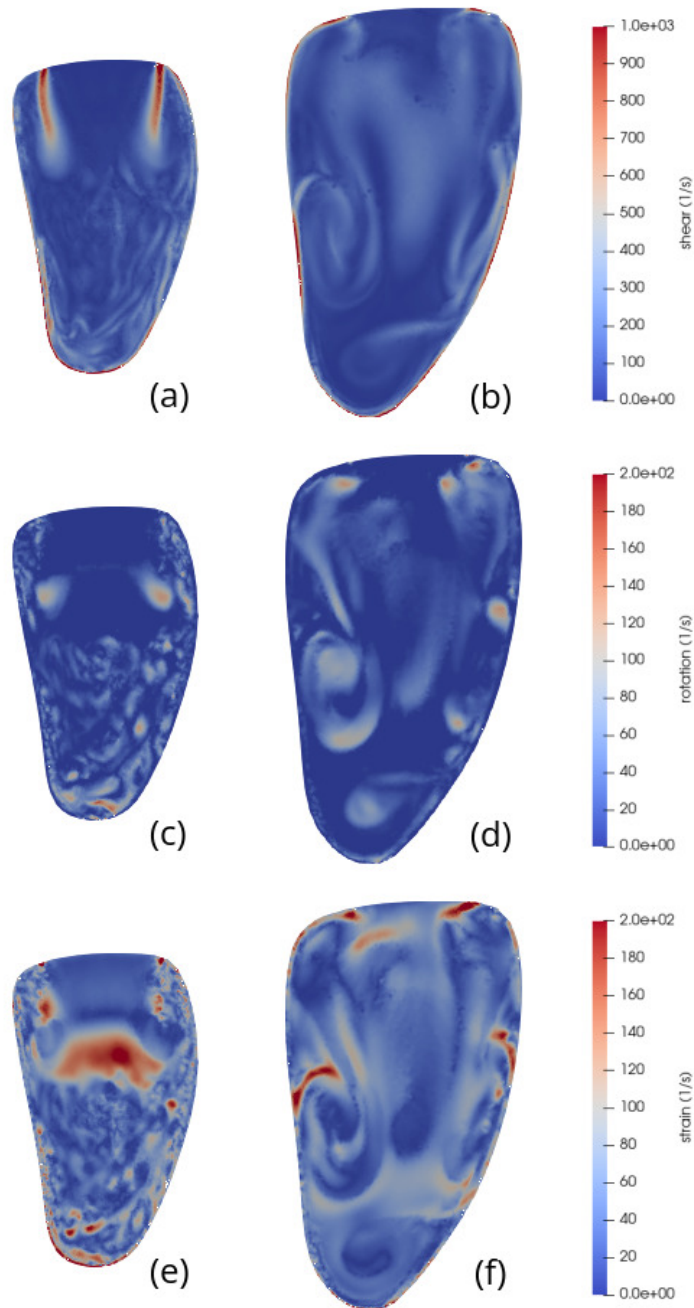


Figure 6. Snapshots of shear flow (a and b), rotational flow (c and d) and straining flow (e and f) at times $t = 0.45$ s (a, c and e) and $t = 0.71$ s (b, d and f) in a vertical bicommissural cut through the left ventricle. This simulation was done with an untreated valve. At time $t = 0.45$ s (early diastole), the flow is dominated by the incoming E-wave jet. The velocity and pressure at this time are shown in figures 4a and 5a respectively. At time $t = 0.71$ s (end diastasis) the inflow jet is weaker, and the initial dominant flow structures of the E-wave have started to break down. Note that the different sizes of the ventricle are due to the diastolic expansion.

299 The strain in the clipped case (figure 7e) is once again large at the bottom of the jet where the inflow
 300 meets slower moving blood. It is also high at the wall in the apical part of the ventricle, and at the edges of
 301 the MV openings. There is also an area of higher strain right in the center of the ventricle, between the two
 302 jets.

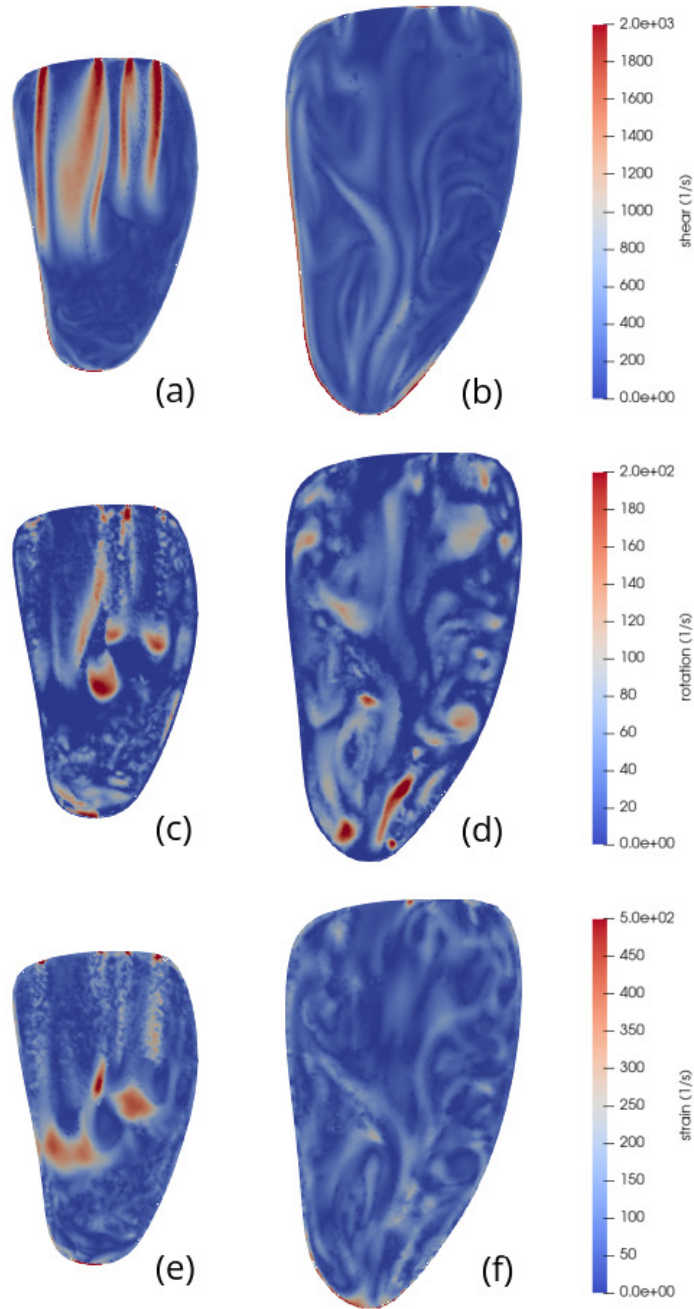


Figure 7. Snapshots of shear (a and b), rotation (c and d) and strain (e and f) at times $t = 0.45$ s (a, c and e) and $t = 0.71$ s (b, d and f) in a vertical bicommissural cut through the left ventricle. This simulation was done with MVC placed at $s \cdot l$ from the center of the coaptation line, with l being the long axis in the MV model, and the position scale factor $s = 0.2$. At time $t = 0.45$ s (early diastole), the flow is dominated by the two incoming E-wave jets. The velocity and pressure at this time are shown in figure 4c and 5c respectively. At time $t = 0.71$ s (end diastasis) the inflow jets are weaker, and the initial dominant flow structures of the E-wave have started to break down. Note that the different sizes of the ventricle are due to the diastolic expansion.

303 At the time of the second snapshot, i.e. the end of diastasis when the strongest effects of the initial E-wave
 304 jets have diminished, the rotation structures are fairly well distributed in the ventricle, with some areas in

305 the apical part of the ventricle where the rotation is relatively high (figure 7d). Much like in the untreated
 306 case, the shear (figure 7b) extends along more parts of the ventricle wall in the second snapshot, with
 307 weaker effects in the interior part. The strain (figure 7f) retains its high magnitude along the apical part of
 308 the ventricular wall.

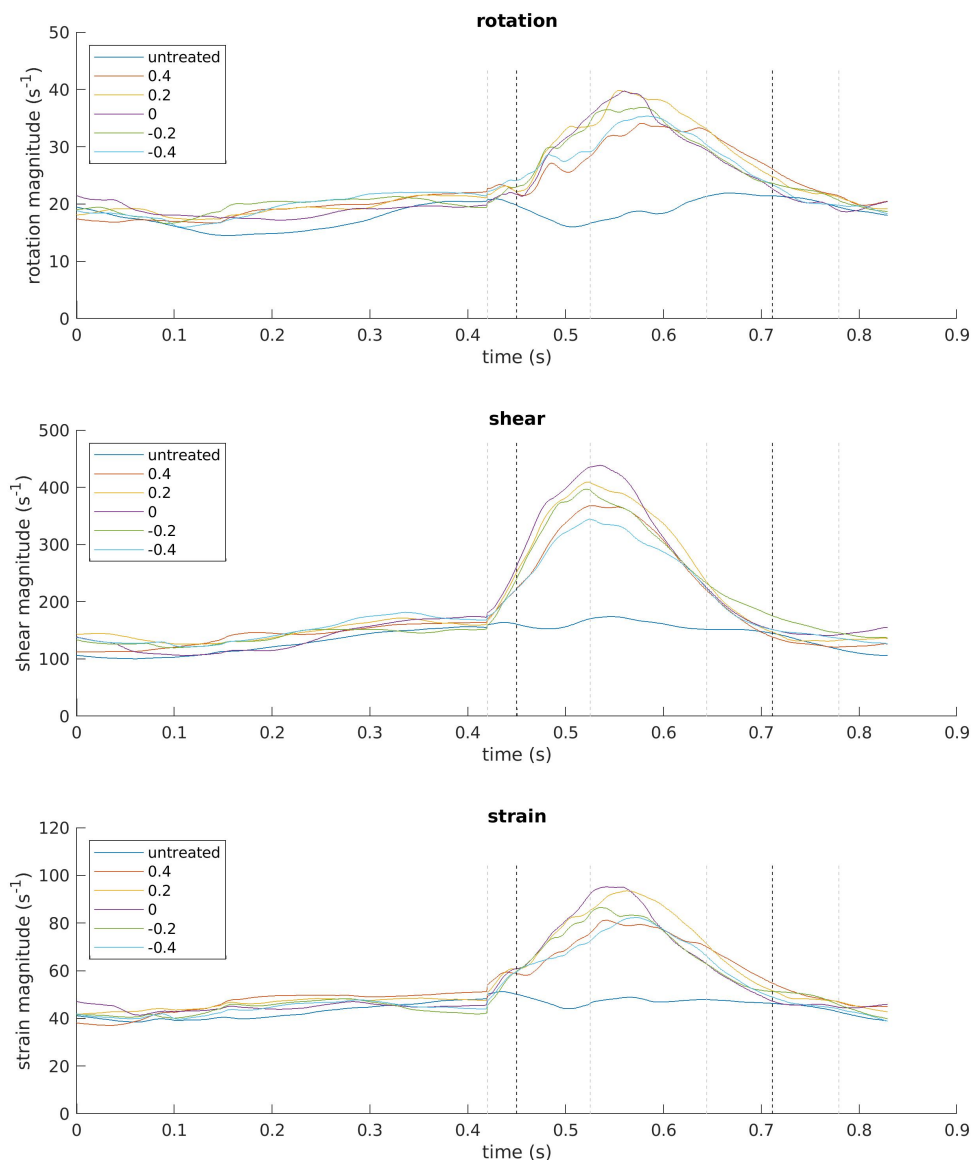


Figure 8. Magnitudes of rotation, shear and strain averaged over the entire ventricle volume and plotted against time over one heartbeat, starting with systole, for all simulated cases. The legend indicates the location of the MVC as relative shift from the center of the coaptation line, except for the healthy (untreated) case. The gray dashed lines mark the time of the start of diastole, E-wave peak, diastasis start, and A-wave peak, also given in table 1. The black dashed lines mark $t = 0.45$ s and $t = 0.71$ s, i.e. the times at which the blood flow is visualized in figures 4, 5, 6, 7, 9 and 10.

309 Differences between the triple decomposition components in the treated and untreated cases include,
310 perhaps most notably, significantly higher magnitudes in strain and shear in the clipped case. The magnitude
311 scales here have been adjusted to better show the location and structures of the different modalities, but
312 figure 8 indicates that the claim holds. In the snapshots of the early diastolic flow, interactions between the
313 two jets in the clipped case give rise to effects not seen in the untreated case, such as the high strain in the
314 center of the ventricle. But vortex rings, high shear along the edge of the jets, and high strain at the bottom
315 of the jets appear in both the treated and untreated cases. Shear and strain along the walls are also prevalent
316 in both cases.

317 To get an idea of the duration and intensity of the different flow modalities from the triple decomposition
318 over a full heartbeat, figure 8 shows the magnitude of the rotation, shear and strain for all simulated cases
319 over time. There are some similarities apparent between all modalities. In systole, they all vary much less
320 than in diastole, with the exception of the untreated case. Across all modalities, the magnitudes in the
321 untreated case peak at much lower values than the MVC cases, despite being at similar levels in systole. It
322 is difficult to distinguish any clear differences between the simulation cases in systole.

323 In diastole, all modalities follow similar temporal patterns in all MVC cases. With the increasing influx
324 of blood in early diastole, the magnitudes of the rotation, shear and strain rise. Shortly after the E-wave
325 peak, the magnitudes also peak and then start to fall. They continue decreasing towards systolic levels, with
326 no real noticeable effects from the A-wave. However, despite having the same inflow volume of blood as
327 the MitraClip cases, the magnitudes of rotation, shear and strain do not rise high above the systolic levels
328 in the untreated case. In fact, after a small initial rise right at the start of diastole, they drop during some of
329 the time leading up to the E-wave peak.

4 DISCUSSION

330 The triple decomposition used here gives an excellent view of the locality and structure of different flow
331 modalities in the LV blood flow. Structures such as strong inflow jets can be visualized and quantified
332 by studying the velocity, and with the addition of pressure, phenomena like the vortex rings around jets
333 can be visualized. However, studying e.g. the shear around the jets requires more sophisticated tools. The
334 triple decomposition captures this, as well as confirms expectations from the velocity and pressure plots.
335 The pressure in the untreated case is relatively low in the basal part of the ventricle, but slightly higher
336 further down. This pattern repeats in the MVC cases, and some of these have even lower pressure where
337 the vortex ring around the inflow jet is expected. The rotation parts (a and b) of figures 6 and 7 confirm that
338 the rotation magnitude is indeed large in those parts. The high strain in the apical part of the ventricle also
339 corresponds well to the high pressure in the same area. A related interesting feature of the rotation and
340 strain is that areas with high rotation often tend to correspond to low strain, and vice versa. An exception to
341 this observation is within the jets, where rotation is 0 and strain is also relatively low. See e.g. figure 6c
342 and e.

343 To get a better idea of some of the 3D structures that appear in the LV flow, and how they develop
344 over time, figure 9 displays snapshots of some 3D structures defined by the computed rotation. Both the
345 untreated and MVC case display clear vortex rings forming around the fronts of the jets as connected
346 structures with rotation magnitude greater than a threshold value of 80 s^{-1} (figure 9a and b). Above these
347 the shear structures are visible at the border around the jet, with significantly higher magnitude in the MVC
348 case. In the rest of the ventricle at this point in time both simulation cases display relatively little rotation,
349 with only small connected volumes reaching above the threshold.

350 At $t = 0.71$ s, when the E-wave jets have decomposed, figure 9c and d gives a very qualitative view of
 351 the distribution of high rotation and shear structures throughout the ventricle. In the untreated case (c), the
 352 rotation appears as connected features, but with very little in the apical part of the ventricle. The shear
 353 is most prominent along the wall. In the clipped case (d), the rotation structures appear more numerous,
 354 and throughout the entire ventricle in different sizes. The shear is again concentrated on the wall, with
 355 higher values as indicated by the color bar. Interestingly, figure 8 at this point in time indicates that the
 356 total amount of rotation/shear magnitudes are similar in both the untreated and clipped ($s = 0.2$) case. We
 357 have not investigated this further, but the reason could be that the more intense patterns visible in the MVC
 358 case make up a relatively small part of the entire ventricle volume, and that the integrated values in figure 8
 359 are thus more strongly influenced by large regions of smaller values.

360 From figure 9 the differences between the distributions of high rotation and shear structures at different
 361 points in time is evident. During the E-wave, much is centered around the jets. Later in diastole, there is a
 362 wider distribution over the ventricle.

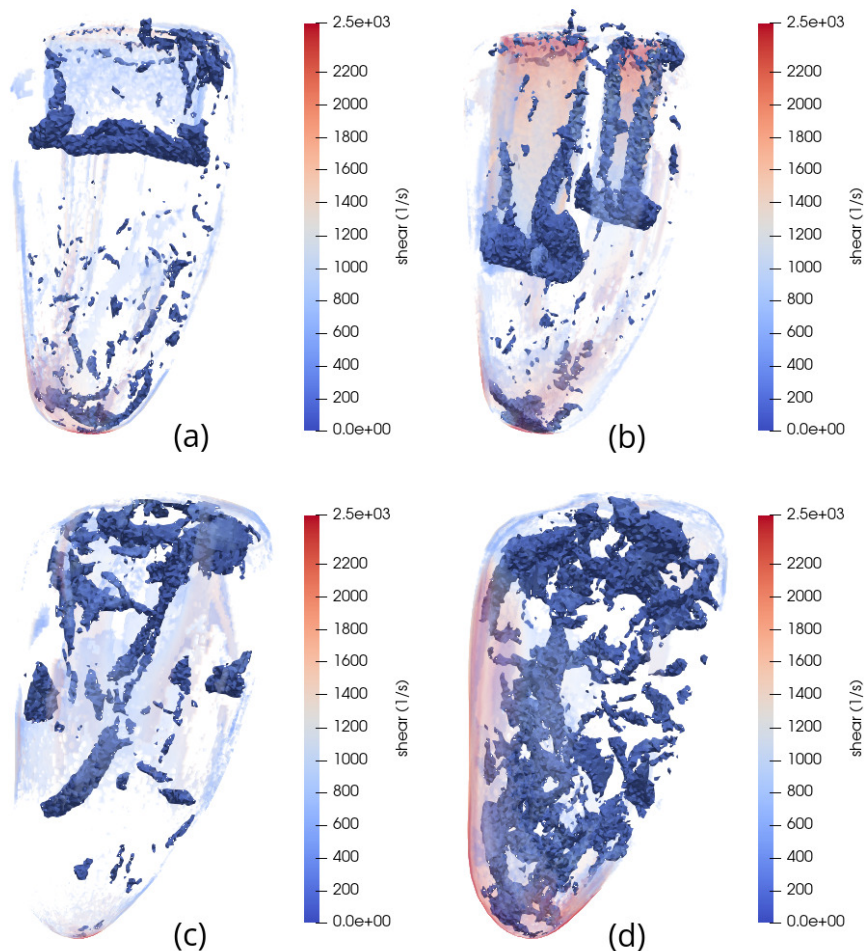


Figure 9. Snapshots of 3D flow structures in the LV blood flow, as determined by the rotation magnitude. The opaque blue structures are all cells that have a rotation magnitude greater than 80 s^{-1} . The transparent structures are cells with shear magnitude greater than 500 s^{-1} , colored in accordance with the color bars. (a) Untreated case, $t = 0.45$ s. (b) MVC case, $s = 0.2$, $t = 0.45$ s. (c) Untreated case, $t = 0.71$ s. (d) MVC case, $s = 0.2$, $t = 0.71$ s. Corresponding 2D snapshots are displayed in figures 6 and 7.

363 Since high shear is known to contribute to thrombosis formation, being able to quantify this in the
364 interventricular blood flow is desirable. Our results suggest that the locations of high shear structures in
365 diastole are similar before and after MVC treatment. They appear mainly around the inflow jets and along
366 the ventricle walls. However, after MVC treatment the magnitude of the shear is higher, possibly as a result
367 of the higher inflow velocities caused by the smaller MV opening areas. As seen in figure 8, the integrated
368 magnitude over the ventricle is higher for all MVC cases than for the untreated case throughout most of the
369 E-wave and diastasis. This implies that the risk of platelets experiencing higher shear which could lead to
370 thrombosis formation is increased after MVC treatment, but further studies would be required to quantify
371 this risk.

372 While shear has been clearly linked to thrombosis formation, the case is more open for strain. Our
373 results indicate that the locations of strain structures, like shear, do not change much in the LV after MVC
374 treatment. But as for shear, strain is higher after treatment, both in maximum magnitude and integrated
375 over the ventricle during the E-wave and diastasis.

376 Since shear, strain and rotation affect platelets differently, it is useful to separate these modalities using
377 the triple decomposition, and be able to study them separately. Often vorticity has been used to similar ends.
378 However, vorticity fails to separate rotation from shear, which can lead to misleading conclusions. Rotation
379 only transports the blood cells, and thus likely does not contribute to platelet activation. Our results clearly
380 show that both shear and rotation are present in the simulated blood flow, but in very different locations
381 and of different magnitudes. Rotation is roughly one order of magnitude lower than shear, and is more
382 prevalent in the vortex ring around the jet, and in connected vortex structures throughout the interior of the
383 ventricle after the strong E-wave jet has diminished.

384 To make a visual comparison between the vorticity and the triple decomposition, figure 10 shows a
385 snapshot of the vorticity for one of the simulated MVC cases, along with the three components from the
386 triple decomposition at the same instant (same as in figure 7a, c and e, but with a logarithmic scale). From
387 this figure it is clear that the vorticity shares similarities with the shear. They reach similar magnitudes, and
388 form structures mainly around the inflow jets and along the walls of the ventricle near the apex. But the
389 logarithmic scale allows for observing the rotation contribution to the flow in the vorticity as well. E.g.
390 the vortex rings show quite clearly as connected areas of high rotation magnitude around the bottom of
391 the jets in figure 10d. (Note also the low strain in the vortex rings in figure 10c.) Since the vortex rings
392 are rotation dominated, they do not show up as clear structures in the shear part (figure 10b). They do
393 however clearly influence the vorticity magnitude around the lower parts of the jets in figure 10a, especially
394 the large rotation structure in the center of the ventricle. Thus using vorticity as a measure of mechanical
395 stimuli on blood cells may lead to inaccurate conclusions. In this particular case the magnitude of the shear
396 is large in comparison to the rotation, which might limit the errors if vorticity were to be used in studies as
397 a substitute for shear. In other settings this may not be the case, or one might be more interested in studying
398 the rotation without influence of the shear. Either way, the triple decomposition offers a very promising
399 way to distinguish rotation and shear in a way that vorticity fails to do.

400 The simulated velocity in the untreated case (figure 4) is within a reasonable range of a healthy heart, but
401 the peak velocities in the clipped cases may be indicative of mitral stenosis Otto et al. (2021). The opening
402 areas of the clipped cases (table 2) are also quite small, and MVC treatment would likely not be clinically
403 considered to mitigate regurgitation if the resulting areas were so small. Nevertheless, increases in inflow
404 velocity as well as the triple decomposition components in the LV following MVC treatment are still likely
405 to appear in clinically realistic cases due to decreased MV area.

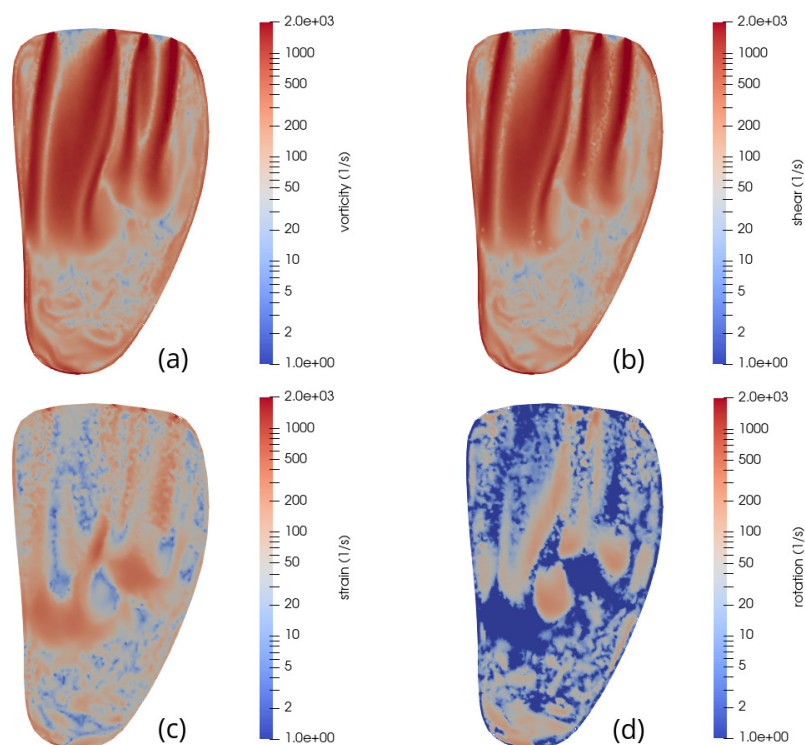


Figure 10. Snapshots of (a) vorticity, (b) shear, (c) strain and (d) rotation at time $t = 0.45$ s in a bicommissural vertical cut through the left ventricle. This simulation was done with a MVC placed at $s \cdot l$ from the center of the coaptation line, with l being the long axis in the MV model, and the position scale factor $s = 0.2$. The velocity and pressure at this time are shown in figure 4c and 5c respectively.

406 While our results show that MVC treatment increases the magnitudes of rotation, shear and strain within
 407 the LV in early diastole, more information is needed to make any claims about the risk of platelet activation
 408 or thrombosis as a consequence of MVC treatment. Not only the magnitude of the shear and strain are
 409 needed to assess such risks, but the duration for which platelets experience these higher levels are of interest
 410 as well. However, studying the magnitude and locations of different flow component structures are an
 411 important first step, which opens up for new opportunities to learn more about mechanical stimuli in blood
 412 flow.

CONFLICT OF INTEREST STATEMENT

413 The authors declare that the research was conducted in the absence of any commercial or financial
 414 relationships that could be construed as a potential conflict of interest.

AUTHOR CONTRIBUTIONS

415 J.K. and J.H. designed the study and the triple decomposition algorithm, and wrote the article. J.K. ran the
 416 simulations and implemented the triple decomposition algorithm. F.S. designed and implemented the MV
 417 model, and D.L. designed and created the diastole timing and axis scaling tool for the MV model. S.E.L.
 418 and L.L. designed and implemented the MVC adaptation of the MV model, and designed the simulation
 419 cases. C.H.P., J.K. and J.H. post-processed and analyzed the results. C.H.P. made the figures in the results
 420 section. J.H. is the PI of the project.

FUNDING AND ACKNOWLEDGEMENTS

421 The authors acknowledge the financial support from the Swedish Research Council (grant number 2018-
422 04854), and the access to computing infrastructure by the Swedish National Infrastructure for Computing
423 (grant number SNIC 2018/3-296).

424 Dr. Lucor has been funded in part by the TOR mobility program of the French Institute of Sweden,
425 dedicated to the improvement of the scientific cooperation between France and Sweden.

REFERENCES

- 426 Adjoua, O. and Lucor, D. (2019). Blood flow reduced-order modeling across macroscopic through
427 mesoscopic scales. In *International Conference on Computational & Mathematical Biomedical*
428 *Engineering*
- 429 Caballero, A., Mao, W., McKay, R., Hahn, R. T., and Sun, W. (2020). A comprehensive engineering
430 analysis of left heart dynamics after mitralclip in a functional mitral regurgitation patient. *Frontiers in*
431 *physiology* 11, 432
- 432 Di Martino, E. S., Guadagni, G., Fumero, A., Ballerini, G., Spirito, R., Biglioli, P., et al. (2001). Fluid-
433 structure interaction within realistic three-dimensional models of the aneurysmatic aorta as a guidance to
434 assess the risk of rupture of the aneurysm. *Medical engineering & physics* 23, 647–655
- 435 Fyrenius, A., Engvall, J., and Janerot-Sjöberg, B. (2001). Major and minor axes of the normal mitral
436 annulus. *The Journal of heart valve disease* 10, 146–152
- 437 Hanségård, J., Urheim, S., Lunde, K., Malm, S., and Rabben, S. I. (2009). Semi-automated quantification
438 of left ventricular volumes and ejection fraction by real-time three-dimensional echocardiography.
439 *Cardiovascular ultrasound* 7, 1–10
- 440 Hiromi Spühler, J. and Hoffman, J. (2021). An interface-tracking unified continuum model for fluid-
441 structure interaction with topology change and full-friction contact with application to aortic valves.
442 *International Journal for Numerical Methods in Engineering* 122, 5258–5278
- 443 Hoffman, J. (2021). Energy stability analysis of turbulent incompressible flow based on the triple
444 decomposition of the velocity gradient tensor. *Physics of Fluids* 33, 081707
- 445 Imanparast, A., Fatourae, N., and Sharif, F. (2016). The impact of valve simplifications on left ventricular
446 hemodynamics in a three dimensional simulation based on in vivo mri data. *Journal of biomechanics* 49,
447 1482–1489
- 448 Kolář, V. (2007). Vortex identification: New requirements and limitations. *International journal of heat*
449 *and fluid flow* 28, 638–652
- 450 Larsson, D., Spühler, J. H., Günyeli, E., Weinkauff, T., Hoffman, J., Colarieti-Tosti, M., et al. (2017a).
451 Estimation of left ventricular blood flow parameters: clinical application of patient-specific cfd
452 simulations from 4d echocardiography. In *Medical Imaging 2017: Ultrasonic Imaging and Tomography*
453 (International Society for Optics and Photonics), vol. 10139, 101390L
- 454 Larsson, D., Spühler, J. H., Petersson, S., Nordenfur, T., Colarieti-Tosti, M., Hoffman, J., et al. (2017b).
455 Patient-specific left ventricular flow simulations from transthoracic echocardiography: robustness
456 evaluation and validation against ultrasound doppler and magnetic resonance imaging. *IEEE transactions*
457 *on medical imaging* 36, 2261–2275
- 458 [Dataset] of Technology, K. R. I. (2021). Beskow. Accessed 2021-04-27
- 459 Otto, C. M., Nishimura, R. A., Bonow, R. O., Carabello, B. A., Erwin, J. P., Gentile, F., et al. (2021).
460 2020 acc/aha guideline for the management of patients with valvular heart disease: A report of the

- 461 american college of cardiology/american heart association joint committee on clinical practice guidelines.
462 *Circulation* 143, e72–e227. doi:10.1161/CIR.0000000000000923
- 463 Pedley, T. J. and Fung, Y. (1980). The fluid mechanics of large blood vessels. *Journal of Biomechanical*
464 *Engineering* 102
- 465 Previtali, E., Bucciarelli, P., Passamonti, S. M., and Martinelli, I. (2011). Risk factors for venous and
466 arterial thrombosis. *Blood Transfusion* 9, 120
- 467 Rahman, S., Fogelson, A., and Hlady, V. (2020). Effects of elapsed time on downstream platelet adhesion
468 following transient exposure to elevated upstream shear forces. *Colloids and Surfaces B: Biointerfaces*
469 193, 111118
- 470 Rojano, R. M., Mendez, S., Lucor, D., Ranc, A., Giansily-Blaizot, M., Schved, J.-F., et al. (2019). Kinetics
471 of the coagulation cascade including the contact activation system: sensitivity analysis and model
472 reduction. *Biomechanics and modeling in mechanobiology* 18, 1139–1153
- 473 Van Loan, C. F. and Golub, G. (1996). Matrix computations (johns hopkins studies in mathematical
474 sciences). *Matrix Computations*
- 475 Westerhof, N., Stergiopoulos, N., Noble, M. I., and Westerhof, B. E. (2010). *Snapshots of hemodynamics:*
476 *an aid for clinical research and graduate education* (Springer)